

Mesoporous Silica Promoted Deposition of Bioinspired Polydopamine onto Contrast Agent: A Universal Strategy to Achieve Both Biocompatibility and Multiple Scale Molecular Imaging

Yu-Wei Chen, Yung-Kang Peng, Shang-Wei Chou, Yu-Jui Tseng, Pei-Chun Wu, Shin-Kung Wang, Yi-Wei Lee, Jing-Jong Shyue, Jong-Kai Hsiao,* Tzu-Ming Liu,* and Pi-Tai Chou*

Polydopamine (PDA) preserves universal coating and metal-binding ability, and is suitable for application in synthesizing multifunctional agents. Herein, utilizing mesoporous silica assisted deposition to enhance both heterogeneous nucleation and loading amounts of PDA, the magnetic resonance (MR) T_1 component (PDA- Fe^{3+}) and MR T_2 /computed tomography (CT)/multiphoton luminescence (MPL) component (FePt) have been successfully integrated in aqueous solution. This four-in-one (T_1 , T_2 , CT, MPL) imaging nanocomposite, FePt@mSiO₂@PDA-polyethylene glycol (PEG), demonstrated its multi-imaging power both in vitro/in vivo. According to our in vitro/in vivo results, FePt@mSiO₂@PDA-PEG reveals water-content-dependent property in T_1 MR imaging, which suggests the necessity of having dual-modal MR ability in a single particle for the precision diagnosis. Most importantly, this dual (T_1 , T_2)-MRI/CT contrast agent is demonstrated complementary to each other in the in vivo testing. PDA coated mesoporous silica also offers an advantage of delayed degradation that prevents adverse effects caused by silica fragments before excretion. The potential of this nanocomposites in both drug carrier and photothermal agent was further evaluated by using doxorubicin and monitoring solution temperature after irradiating 808 nm continuous-wave, respectively. The merits of controlled polymerization, enhanced PDA loading, and biofavorable degradation make this methodology promising to other nanoparticle@mSiO₂ for a wide range of bioapplications.

1. Introduction

Nowadays, imaging tools such as magnetic resonance imaging (MRI), computed tomography (CT), positron emission tomography, and multiphoton luminescence (MPL) have been widely used in clinical research. As each technique has its own merit and limitation, a single-injected contrast agent that can simultaneously response to different imaging tools has become a strategy to design a multimodality imaging nanoparticle (NP).^[1] For instance, MRI has the advantage of soft tissue imaging, noninvasive manner, and high spatial resolution while CT costs less and is more sensitive to bone structures. The combination of these two contrast agents (MRI/CT) is therefore complementary and many studies have successfully prepared either T_2 /CT^[2] or T_1 /CT^[3] bimodal contrast agents during the past decade. However, the ubiquitously used MR components such as iron oxide NP-based T_2 contrast agents (negative contrast) and Gd³⁺-based T_1 complexes

Y.-W. Chen, Y.-K. Peng, Dr. S.-W. Chou, Y.-J. Tseng, Prof. P.-T. Chou
Department of Chemistry
National Taiwan University
10617 Taipei, Taiwan
E-mail: chop@ntu.edu.tw

P.-C. Wu, Prof. T.-M. Liu
Institute of Biomedical Engineering
National Taiwan University
Taipei 10617, Taiwan
E-mail: f88941002@gmail.com

P.-C. Wu, Prof. T.-M. Liu
Molecular Imaging Center
National Taiwan University
Taipei 10617, Taiwan

S.-K. Wang, Y.-W. Lee, Prof. J.-J. Shyue
Department of Materials Science and Engineering
National Taiwan University
Taipei 10617, Taiwan

DOI: 10.1002/ppsc.201600415

S.-K. Wang, Y.-W. Lee, Prof. J.-J. Shyue
Research Center for Applied Science
Academia Sinica
Taipei 11529, Taiwan

Dr. J.-K. Hsiao
Department of Medical Imaging
Taipei TzuChi Hospital
The Buddhist Tzuchi Medical Foundation
Taipei 23142, Taiwan
E-mail: jongkai@tzuchi.com.tw

Dr. J.-K. Hsiao
School of Medicine
Tzu-Chi University
Hualien 97004, Taiwan



(positive contrast) proved to have serious adverse effects (cf. CT component). Despite its high biocompatibility, the former can induce long range magnetic field and the susceptibility artifacts, which distort the background image, leading to the difficulty in differentiation between contrast agents and artifacts.^[4] The latter can provide positive contrast but may cause fatal nephrogenic systemic fibrosis and difficulty in metabolism.^[5] Furthermore, a single mode contrast in MRI has recently been found not yet perfect and is increasingly facing challenges, especially when more accurate imaging and sufficient contrast are required for small biological targets. A biocompatible MRI/CT contrast agent that can provide MR contrast in both T_1 - and T_2 - weighted imaging is thus preferred.

Even though several studies have attempted to prepare T_1/T_2 dual-modal contrast agent (DMCA) for use in MRI,^[6] the integrating T_1/T_2 into one nanoplatform has been a challenging task as the proximity between T_1 and T_2 materials would cause magnetic quenching effect,^[6d] making it difficult to synthesize MR DMCA with high efficiency. Accordingly, Cheon and co-workers proposed a “magnetically decoupled” core-shell design concept to optimize a MR DMCA. They demonstrated that the degree of coupling between T_2 core ($MnFe_2O_4$) and T_1 shell ($Gd_2O(CO_3)_2$) can be modulated by using a 16 nm separating silica layer, which makes it possible to optimize T_1 and T_2 signals.^[6d] Further changes of the shell paramagnetic materials to $Mn(BTC)(H_2O)$ have also been made to fine-tune T_1 and T_2 signals,^[6h] but the toxicity issues cannot be completely ruled out. For example, the brain is particularly vulnerable to high concentration of manganese exposure, which can cause a neurodegenerative disorder known as “manganism” with Parkinson-like symptoms.^[7] In theory, ferric ions (Fe^{3+}) having five unpaired electrons can increase the r_1 value, for which the biocompatibility is superior to Gd- or Mn-based materials due to its ubiquity in the living system.^[8] Unfortunately, their associated iron oxide nanoparticles possess high saturation magnetization (M_s) and therefore high r_2 ($r_2 \propto M_s$), which are not appropriate for T_1 contrast agents due to the large r_2/r_1 ratio.^[9] It is not until recently that chelating iron ions with polydopamine (PDA), a mussel-inspired material, efficiently promoted the longitudinal relaxation (T_1) of water proton.^[10] According to SBM (Solomon-Bloembergen-Morgan) theory,^[11] this contrast enhanced capability can be attributed to the increase in both longitudinal inner- and outer-sphere relaxivity.

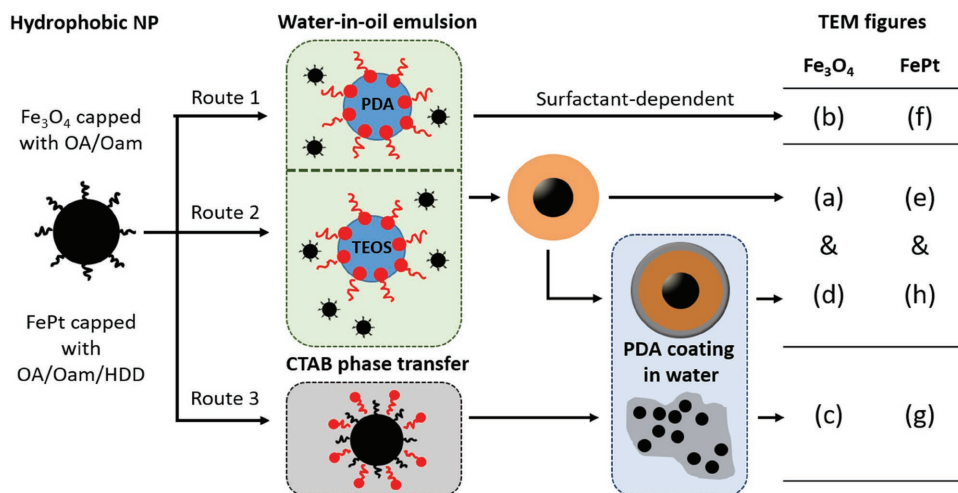
Very recently, a well-defined PDA shell coating on manganese oxide nanoparticle ($MnO@PDA$) can be easily prepared by water-in-oil microemulsion method as the polymerization of dopamine is confined in the water nanodroplet.^[12] However, this method is only applicable for the incorporation of specific NPs (vide infra) presumably due to the replacement of surfactant by hydrolyzed dopamine species in the intermediate process.^[13] Even though several attempts have been made to prepare $NP@PDA$ in pure water phase, due to the unconfined polymerization of dopamine, a strictly controlled reaction that favors heterogeneous rather than homogeneous nucleation is required to deposit a uniform layer on NP.^[14] As the preparation in water phase is more favorable for biomaterials, a facile method to deposit a well-defined PDA on functional NPs is thus highly desirable.

In this study, first, we demonstrate that the heterogeneous nucleation of dopamine in aqueous solution can be largely promoted by the deposition of a silica layer on NP (cf. bare NP). To achieve multiscale imaging and high biocompatibility, this strategy was then adopted to integrate the T_1 component (PDA- Fe^{3+}) and T_2 /CT/MPL component ($FePt$)^[15] in aqueous solution, forming a four-modalities-in-one contrast agent (denoted as $FePt@mSiO_2@PDA$, $mSiO_2$: mesoporous silica). To the best of our knowledge, there is no integration of either CT or MPL component into MR DMCA reported so far. In our design, the interlayer mesoporous silica separates two domains, i.e., interior core and outer shell, which can be functionalized independently and therefore spatially separate T_2/T_1 material. The high surface area of mesoporous silica interlayer not only promotes the heterogeneous nucleation of dopamine but also helps enhancing polydopamine- Fe^{3+} loading and therefore improves T_1 contrast (cf. nonporous silica coating). Further modification was made by encapsulating methoxy polyethylene glycol thiol (mPEG-SH) via Michael addition for longer blood circulation time in vivo.^[16] The final product, $FePt@mSiO_2@PDA-PEG$, showed its versatility and synergetic effect in in vivo T_1/T_2 /CT/MPL imaging. Especially, the water-content-dependent property in T_1 -weighted MR imaging strongly suggests the necessity of having dual-modal MR imaging ability in a single particle for the precision diagnosis. Furthermore, this dual(T_1, T_2)-MRI/CT contrast agent is demonstrated complementary to each other in our in vivo testing. We also investigate the correlation for biodegradation versus different nanocomposites ($mSiO_2$, $FePt@mSiO_2$, $FePt@mSiO_2@PDA$) and showed that PDA incorporated $FePt@mSiO_2@PDA$ can reduce silica degradation before excretion, rendering functional integrity. In the preliminary test of therapeutics, we further loaded doxorubicin (DOX) onto $FePt@mSiO_2@PDA-PEG$ and evaluated its potential as a drug carrier. Also, the photothermal effect was measured by the detection of temperature elevation of $FePt@mSiO_2@PDA$ after irradiating 808 nm continuous-wave (1 W cm^{-2}). Details of results, discussion, and perspectives are elaborated in the following sections.

2. Results and Discussion

2.1. Silica Assisted Heterogeneous Nucleation of Dopamine

Given that the water droplet in water-in-oil microemulsion acts as a confined nanoreactor for the polymerization of tetraethyl orthosilicate (TEOS), the deposition of a well-defined silica layer on various hydrophobic NPs ($NP@SiO_2$) has been achieved during the past decade (Scheme 1: route 2).^[6a,b,13] This facile preparation of nearly single core $NP@SiO_2$ was demonstrated on two materials in this study: Fe_3O_4 ($Fe_3O_4@SiO_2$ (Figure 1a)) and $FePt$ ($FePt@SiO_2$ NPs (Figure 1e)). The hydrolyzed TEOS species were found playing an important role in replacing hydrophobic surfactants on NP for the transfer from oil phase into water droplets.^[13] Very recently, Zhang and co-workers successfully prepared $MnO@PDA$ by the confined polymerization of dopamine in the water droplet (Scheme 1: route 1).^[12] However, only ill-defined $Fe_3O_4@PDA$ was prepared (Figure 1b) and no $FePt$ NP being transferred into water



Scheme 1. Illustration of PDA coating experiments carried out in Figure 1 (OA: oleic acid; Oam: oleylamine; HDD: 1,2-hexadecandiol).

droplet could be observed (Figure 1f) presumably due to the fact that the hydrolyzed dopamine is not strong enough to replace the surfactant (i.e., 1,2-hexadecandiol, HDD) on FePt NP (cf. Fe₃O₄).

To evaluate the coating of PDA on NPs in pure water phase, those hydrophobic Fe₃O₄ and FePt NPs were further transferred to hydrophilic phase with the assist of cetyltrimethylammonium bromide (CTAB). No aggregation is observed for both water-dispersed Fe₃O₄ and FePt NPs (Figure S1, Supporting Information). The polymerization of dopamine on these hydrophilic NPs was initiated by adding 1 N NaOH(aq). As expected, the self-polymerization of dopamine in the unconfined water phase

(Scheme 1: route 3) generated large Fe₃O₄/PDA (Figure 1c) and FePt/PDA (Figure 1g) aggregates (cf. water-in-oil microemulsion method, Figure 1b,f). This self-polymerization of dopamine was found to be strongly suppressed by the introduction of a silica layer on NPs under the same reaction condition (see Figure 1d (Fe₃O₄@SiO₂@PDA) and Figure 1h (FePt@SiO₂@PDA)). Given that -OH groups of silica can stabilize dopamine via hydrogen bonding formation,^[17] dopamine thus tends to heterogeneously nucleate and subsequently grows a layer on the silica surface instead of random self-polymerization. In our aim to achieve multiscale imaging agent, we then focus on FePt core, which is a promising material in T₂-weighted MRI,

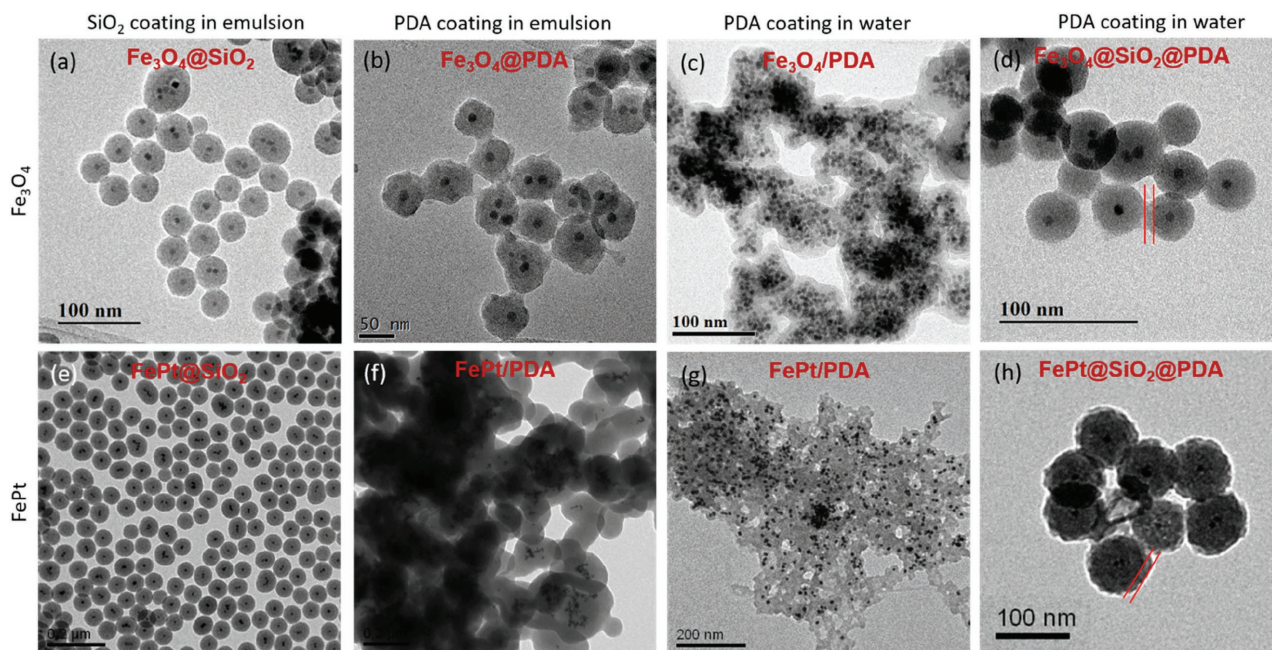
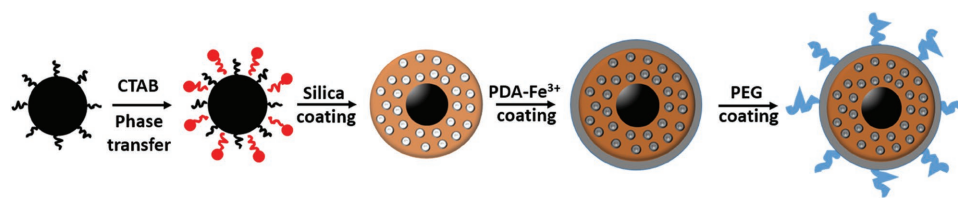


Figure 1. Deposition of silica by water-in-oil microemulsion on a) Fe₃O₄ and e) FePt, followed by PDA coating (indicated by red line) in water phase on d) Fe₃O₄@SiO₂ and h) FePt@SiO₂. Deposition of PDA by water-in-oil microemulsion on b) Fe₃O₄ and f) FePt and PDA coating in water phase on c) Fe₃O₄ and g) FePt.



Scheme 2. Illustration of preparation for FePt@mSiO₂@PDA-PEG NPs.

CT, and MPL imaging,^[15] and its integration with T₁ material (PDA-Fe³⁺) described in the following experiments.

2.2. Detailed Synthesis and Characterization of FePt@mSiO₂@PDA-PEG NPs

As the increase of surface OH concentration is believed to promote the heterogeneous nucleation of dopamine on silica, we then employed mesoporous silica (mSiO₂) as the interlayer. The preparation of FePt@mSiO₂@PDA-PEG is schematically illustrated in **Scheme 2**. Briefly, the as-prepared hydrophobic FePt NPs were transferred into hydrophilic phase with the assist of CTAB. CTAB molecules herein served as templates for the formation of mesoporous silica shell on FePt NPs, and were later removed by ion exchange with NH₄NO₃ to form void channels. The structure of FePt@mSiO₂ is confirmed by transmission electron microscopy (TEM) as shown in **Figure 2a**. The average size of FePt@mSiO₂ is 87.6 ± 6.5 (σ: 8.63%) nm calculated from TEM images (see Figure S2a in the Supporting Information). As evidenced by **Figure 2b**, a well-defined PDA layer (≈20 nm) was successfully deposited on FePt@mSiO₂. The average size of FePt@mSiO₂@PDA is around 143 ± 12 (σ: 7.35%) nm (**Figure S2b**, Supporting Information). In stark contrast, for FePt without silica coating, random self-polymerization of dopamine in water was found (**Figure 1g**). As a result, the high density of hydroxyl group in mesoporous silica shell indeed provides an alternative thermodynamically favored environment for the heterogeneous nucleation of dopamine (cf. random self-polymerization) that no strictly control needed.

X-ray powder diffraction patterns of FePt@mSiO₂ and FePt@mSiO₂@PDA are shown in **Figure S3** (Supporting Information), in which two diffraction peaks at 2θ around 40° and 47° come from (111) and (200) facet of fcc structure of the FePt NP. The broad band where 2θ range from 20° to 30° is due to the amorphous property of mesoporous silica and polydopamine. Energy-dispersive X-ray spectroscopy (EDS) was further performed to confirm Fe/Pt/Si/O elements in FePt@mSiO₂ (see **Figure S4** in the Supporting Information). The successful coating of polydopamine-Fe³⁺ was supported by secondary ion mass spectrometer (SIMS) (**Figure 3a,b**), in which the peak at *m/z* = 152.05 represents the fragments originating from the polydopamine building block, while peak of Fe only appears after cleaving Fe³⁺, demonstrating the chelation of Fe³⁺ ions by catechol moiety of PDA component of FePt@mSiO₂@PDA. The

observation of Fe/C/N/O peaks in X-ray photoelectron spectroscopy (XPS) (**Figure S5**, Supporting Information) also supports the coating of PDA-Fe³⁺.

In an aim to investigate longitudinal (T₁)/transverse (T₂) relaxation time versus core materials and shell silica porosity, we then systematically measured the longitudinal/transversal relaxivity as a function of the following nanoparticles, namely FePt@SiO₂@PDA, Fe₃O₄@SiO₂@PDA, and FePt@mSiO₂@PDA. Based on the *r*₁ and *r*₂ relaxivity values listed in **Table 1**, FePt@mSiO₂@PDA reveals highest *r*₁ (3.502 mm⁻¹ s⁻¹) with *r*₂/*r*₁ ratio of 2.048. Comparing to FePt@SiO₂@PDA with non-porous silica (*r*₁ = 1.119), the tripled *r*₁ value is attributed to the increased polydopamine-Fe³⁺ loading via the mesoporous structure. While changing the core to Fe₃O₄ (i.e., Fe₃O₄@SiO₂@PDA), the intrinsic strong magnetization of iron oxide (**Figure S6**, Supporting Information) disturbs the relaxation of T₁ shell and tends to become a more T₂ dominant contrast agent (with the highest *r*₂/*r*₁ ratio).

The corresponding MRI phantom images of these three NPs are shown in **Figure 4**. As expected, the low magnetization of FePt in FePt@mSiO₂@PDA gives dual T₁/T₂ imaging (**Figure 4a**) without the quenching of T₁ signal (cf. Fe₃O₄@SiO₂@PDA, **Figure 4b**) and renders a stronger T₁ contrast (cf. FePt@SiO₂@PDA, **Figure 4b**). Moreover, the T₁ MR imaging of FePt@mSiO₂@PDA decreases when [Fe] increases from 0.83 × 10⁻³ to 2.51 × 10⁻³ M. The decreased T₁ imaging contrast at high concentration has been a known phenomenon, which is associated with the generation of local magnetic field distortion at high local concentration.^[6h,18] The CT imaging ability of FePt@mSiO₂@PDA was also evaluated. As shown in **Figure 4c**, the enhancement in CT becomes stronger when particle concentration is increased. This trend is similar to the MR T₂ imaging and the results suggest that both T₂ and CT

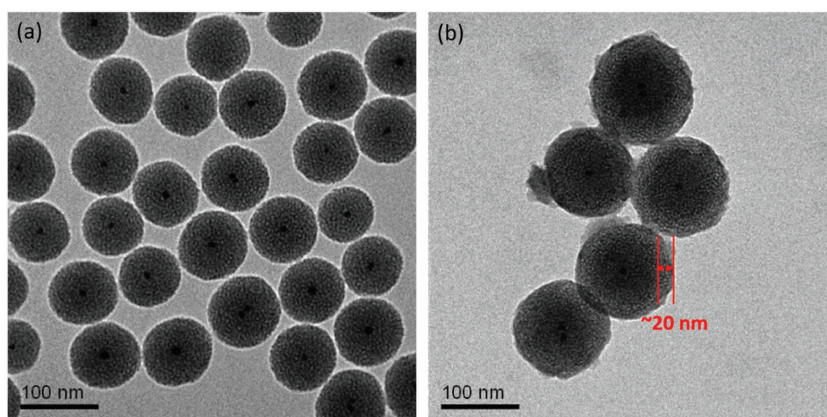


Figure 2. The TEM images of a) FePt@mSiO₂ and b) FePt@mSiO₂@PDA.

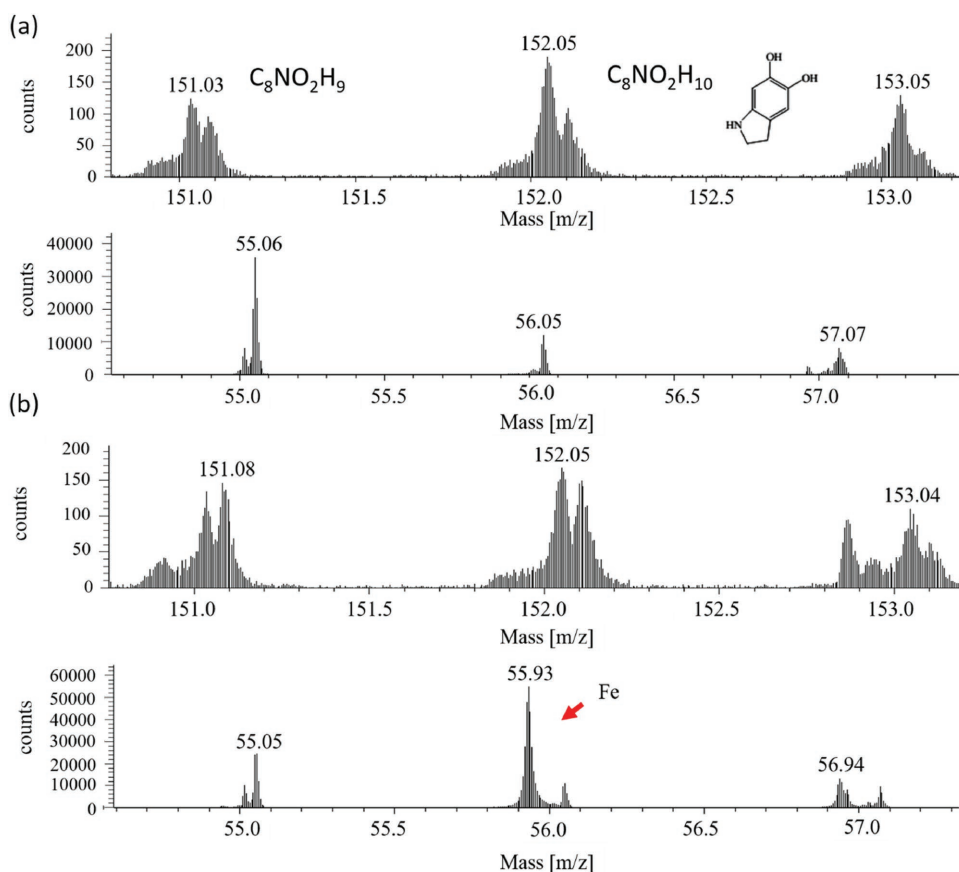


Figure 3. The SIMS spectra of a) FePt@mSiO₂@PDA (before cleating Fe³⁺) and b) FePt@mSiO₂@PDA after binding Fe³⁺.

contrasts mainly come from the FePt core while T₁ mainly originates from the shell part polydopamine-Fe³⁺.

2.3. Biodegradability Test

How nanoparticles are metabolized after being injected into the body is of prime importance when they come to biological applications. It has been reported that protein existing in serum with strong Fe³⁺ binding affinity (e.g., transferrin, $K_d = 10^{-22}$ M) could help removing the Fe³⁺ ions doped in hollow silica nanoshells, thereby accelerating the collapse of the silica frameworks.^[19] In our previous work, this biodegrading process also applies to mesoporous silica where the outward diffusion of Fe³⁺ ions (Kirkendall process) results in the shrinkage of interior silica framework and leads to degradation of particles.^[8,20] To the best of our knowledge, no relevant study toward biodegradation

Table 1. The relaxivity of FePt@SiO₂@PDA, Fe₃O₄@SiO₂@PDA, and FePt@mSiO₂@PDA.

	r_2 [mM ⁻¹ s ⁻¹]	r_1 [mM ⁻¹ s ⁻¹]	r_2/r_1
FePt@SiO ₂ @PDA	1.825	1.119	1.631
Fe ₃ O ₄ @SiO ₂ @PDA	6.946	0.924	7.517
FePt@mSiO ₂ @PDA	7.173	3.502	2.048

on such iron-ion based core-silica/PDA-Fe³⁺ shell system has been reported. It is also interesting to know whether the PDA coating can have any influence on this process. To investigate the correlation for biodegradation versus nanocomposites, we dispersed mSiO₂, FePt@mSiO₂, FePt@mSiO₂@PDA in both fetal bovine serum (FBS) (containing transferrin) and phosphate buffer saline (PBS) (at 37 °C) and monitored corresponding morphological transformation after 24 h and 3 d.

For pure silica (i.e., mSiO₂), as predicted, there is negligible morphology change in both PBS and FBS (Figure 5a). In contrast, the silica shell of FePt@mSiO₂ has been degraded with FePt nanoparticles spread out (in red circle) from the silica frameworks after 3 d of incubation in FBS (Figure 5b). It is surprising that the PDA-Fe³⁺ coated FePt@mSiO₂@PDA maintains most of its morphology after 3 d of incubation in FBS (Figure 5c). This “delayed-degradation” is believed to be due to the iron (III) binding affinity ($K_d = 13 \times 10^{-9}$ M) of polydopamine,^[21] which slows down the outward diffusion of Fe³⁺ ions. Further support of this viewpoint was given by the lack of apparent morphology changes for both PDA (Figure S7, Supporting Information) and PDA-Fe³⁺ particles (Figure S8, Supporting Information) after 3 d of incubation in FBS.

We further evaluated how long PDA-Fe³⁺ could maintain the structure after treating with FBS. As shown in Figure 5d, the shrinkage of interior silica of FePt@mSiO₂@PDA could be found after 5 d of incubation in FBS, which almost lost its morphology after 7 d of incubation. This result on the one hand

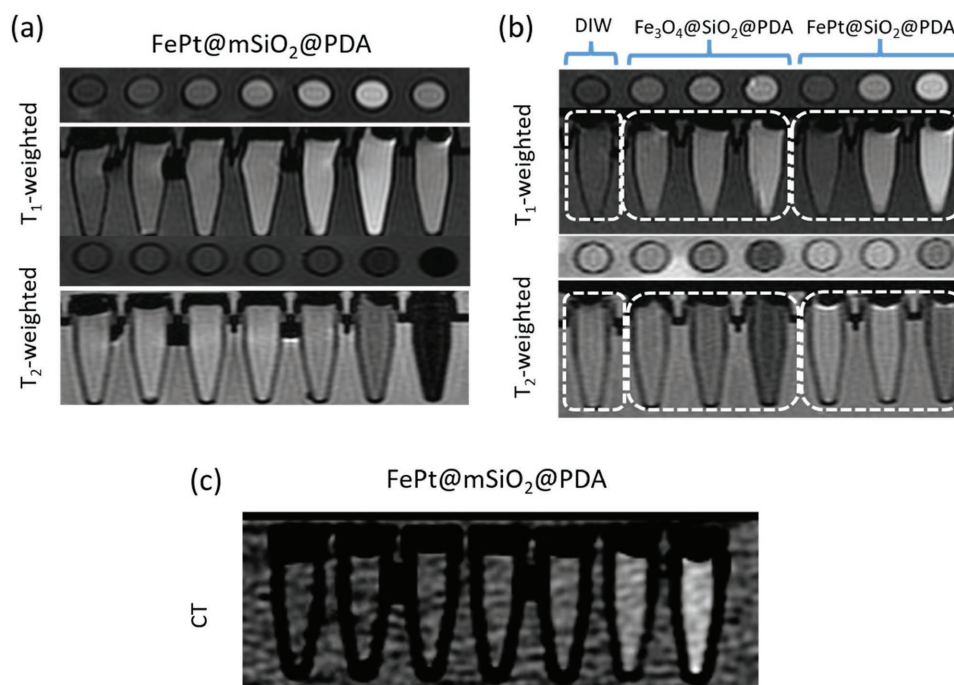


Figure 4. T_1 and T_2 MR images of a) $\text{FePt@mSiO}_2\text{@PDA}$ and b) $\text{FePt@SiO}_2\text{@PDA}$ and $\text{Fe}_3\text{O}_4\text{@SiO}_2\text{@PDA}$. c) The CT image of $\text{FePt@mSiO}_2\text{@PDA}$. Note that the Fe concentration (from left to right) is 0, 0.0636×10^{-3} , 0.126×10^{-3} , 0.257×10^{-3} , 0.425×10^{-3} , 0.828×10^{-3} , 2.51×10^{-3} M in (a); 1.54×10^{-3} , 2.23×10^{-3} , 3.26×10^{-3} M for $\text{Fe}_3\text{O}_4\text{@SiO}_2\text{@PDA}$, and 0.245×10^{-3} , 0.526×10^{-3} , and 1.18×10^{-3} M for $\text{FePt@SiO}_2\text{@PDA}$ in (b). The Pt concentration from left to right in (c) is 0×10^{-3} , 0.198×10^{-3} , 0.549×10^{-3} , 1.20×10^{-3} , 2.16×10^{-3} , 3.34×10^{-3} , and 7.02×10^{-3} M.

suggests that the resistance of $\text{FePt@mSiO}_2\text{@PDA}$ to FBS can delay the degradation of silica and hence maintain its integrity, such that the generation of toxic silica oligomers before excretion can be prevented. On the other hand, the nanocomposite is not too robust and is still degradable, avoiding long-term accumulation.

2.4. In Vitro MR and CT Testing

Since molecules with $-\text{SH}$ or $-\text{NH}_2$ functional groups can be easily attached to dopamine through Michael addition, mPEG-SH was further modified on $\text{FePt@mSiO}_2\text{@PDA}$ to ensure better dispersity (Figure S9, Supporting Information) and longer blood circulation span before in vitro/in vivo test.^[16] The successful PEG modification was confirmed by Fourier transform infrared spectra (FTIR) shown in Figure S10 (Supporting Information). The in vitro cytotoxicity of $\text{FePt@mSiO}_2\text{@PDA-PEG}$ was then evaluated by MTT (3-(4, 5-dimethylthiazol-2-yl)-2,5-diphenyltetrazolium bromide) assay to evaluate its biocompatibility to the cells. As shown in Figure 6a, the negligible cytotoxicity of $\text{FePt@mSiO}_2\text{@PDA-PEG}$ with concentration up to $200 \mu\text{g mL}^{-1}$ (all groups have cell viability above 90%) suggests high biocompatibility of this nanocomposite to cells. In vitro MRI and CT testing was evaluated by feeding $\text{FePt@mSiO}_2\text{@PDA-PEG}$ to HeLa cells for 3 h and washed several times to assure that the MR/CT imaging contrast effects are from those particles taken up by cells.

As shown in Figure 6b, both T_2 -weighted MR and CT contrasts enhance as the intake of particle increases. However, T_1 -weighted MR signal intensity starts to decrease when [Fe]

concentration increases to 0.10×10^{-3} M and even turns lower at 0.14×10^{-3} M. The lower [Fe] threshold (0.10×10^{-3} M) compared to previous tube imaging (Figure 4a) is attributed to the accumulation of internalized particles in HeLa cell. This result suggests that the dispersity of contrast agent in vivo under T_1 -weighted MR imaging should be evaluated carefully as the water content varies from organ to organ (vide infra). To show both MR/CT signals originating from $\text{FePt@mSiO}_2\text{@PDA-PEG}$ NPs uptaken by HeLa cell, Prussian blue staining was carried out to locate the Fe^{3+} ions of $\text{FePt@mSiO}_2\text{@PDA-PEG}$. As shown in Figure S11b (Supporting Information), blue staining can be seen for cells treated with $\text{FePt@mSiO}_2\text{@PDA-PEG}$ while none of such staining is observed for cells fed with PBS buffer (Figure S11a, Supporting Information).

2.5. In Vivo MR, CT, and Multiphoton Imaging

The MR in vivo experiment was carried out by intravenous administration of $\text{FePt@mSiO}_2\text{@PDA-PEG}$ into the mice tail vein and monitoring their MRI response at different time intervals. It is noted that the apparent T_1 enhancement can be seen in the bladder (Figure 7a) but not for T_2 . Conversely, T_2 enhancement is obvious in liver and kidney (Figure 7b) 1 h after injection. This result is in line with previous in vitro experiments where we have observed that the T_1 MR contrast could vanish when the local concentration of $\text{FePt@mSiO}_2\text{@PDA-PEG}$ exceeded the threshold. To be more specific, as liver possesses less water (cf. bladder) no T_1 and only T_2 enhancement is observed (Figure 7c). The disappearance of T_1 signal

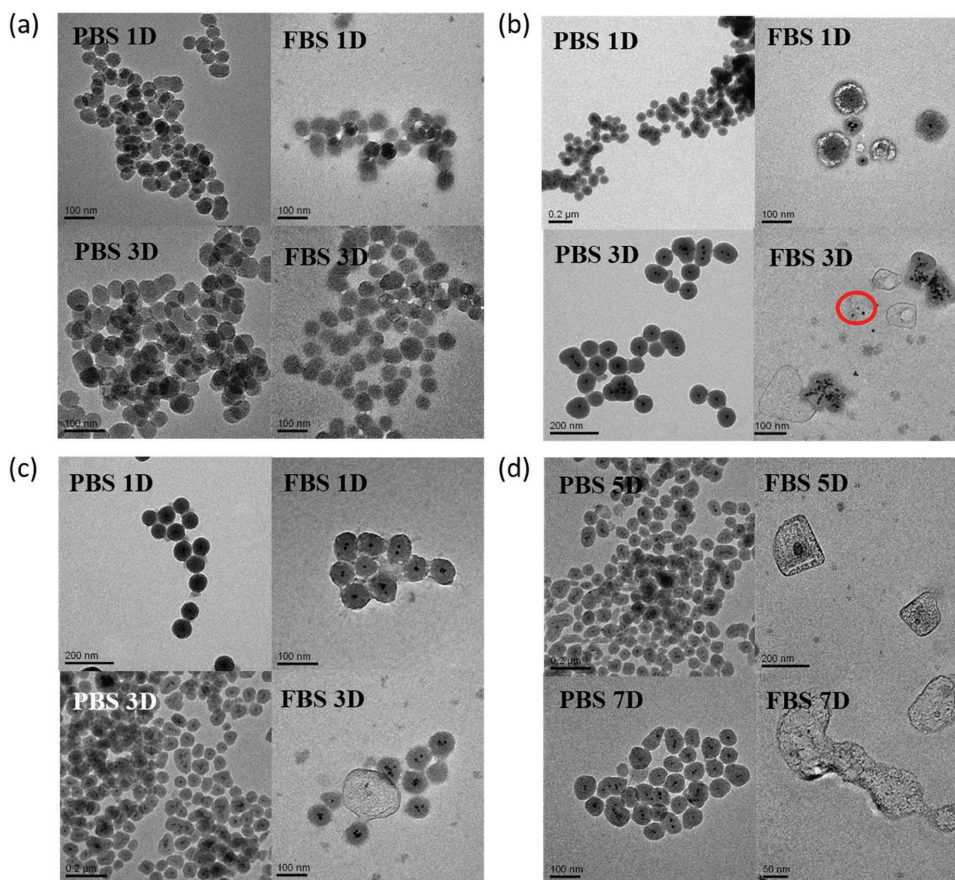


Figure 5. The TEM images of a) $mSiO_2$, b) $FePt@mSiO_2$, c) $FePt@mSiO_2@PDA$ treated with PBS (left) and FBS (right) for 1 (upper) and 3 d (lower), and d) $FePt@mSiO_2@PDA$ treated with PBS and FBS for 5 (upper) and 7 d (lower).

of $FePt@mSiO_2@PDA-PEG$ in liver is attributed to the over-threshold particle concentration. When these particles flow into a water-rich organ bladder (cf. liver), a clear T_1 signal is regained as the concentration of $FePt@mSiO_2@PDA-PEG$ is now below the threshold. Unfortunately, the T_2 signal in bladder is difficult to evaluate as the bright background of this organ under T_2 -weighted mode (Figure 7a).

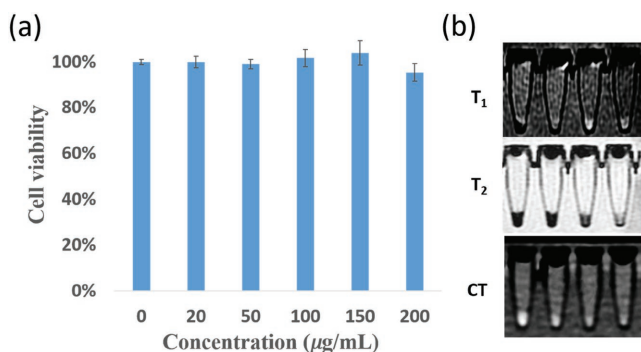


Figure 6. a) The cell viability test of $FePt@mSiO_2@PDA-PEG$. b) The MR and CT images of $FePt@mSiO_2@PDA-PEG$ in vitro. The Fe concentration (left to right) is 0.14×10^{-3} , 0.10×10^{-3} , 0.02×10^{-3} , and 0.005×10^{-3} M. The Pt concentration (left to right) is 0.14×10^{-3} , 0.072×10^{-3} , 0.017×10^{-3} , and 0.006×10^{-3} M.

The all above liver/bladder observation can be further supported by the kidney MR imaging of pelvis (water-rich), cortex, and medulla (water-scant) (Figure 7b). No apparent T_1 signal could be observed in both cortex and medulla but pelvis under T_1 -weighted mode (Figure 7d). Conversely, T_2 enhancement appeared in both cortex and medulla but not pelvis under T_2 -weighted mode. These results evidently demonstrate that some of our PEG-modified particle (even size > 100 nm) can escape the surveillance of the reticuloendothelial system from the liver and can be further secreted by kidneys and then in the bladder.^[8,22] All these in vivo MR results again imply that a single mode contrast in MRI is not yet sufficient. A contrast agent that can respond dual T_1/T_2 mode in MR diagnosis is much preferred for the precision diagnosis. Potentially, it is a powerful tool to detect liver cancer, urinary tract stone, or malignancy under MRI which is clinically demanding.

In vivo CT test was also carried out and the results are summarized in Figure 8a,b. As shown in Figure 8b, the bladder reveals a nearly twice CT enhancement after 40 min intravenous tail injection. As this contrast comes from the core FePt, the result suggests that the $FePt@mSiO_2@PDA-PEG$ particles stay in one unity over the span of imaging as well as affirms that previous MR results do not originate from either FePt NP in liver or degraded PDA in bladder. Most importantly, the appearance of this CT signal in bladder not only supports our

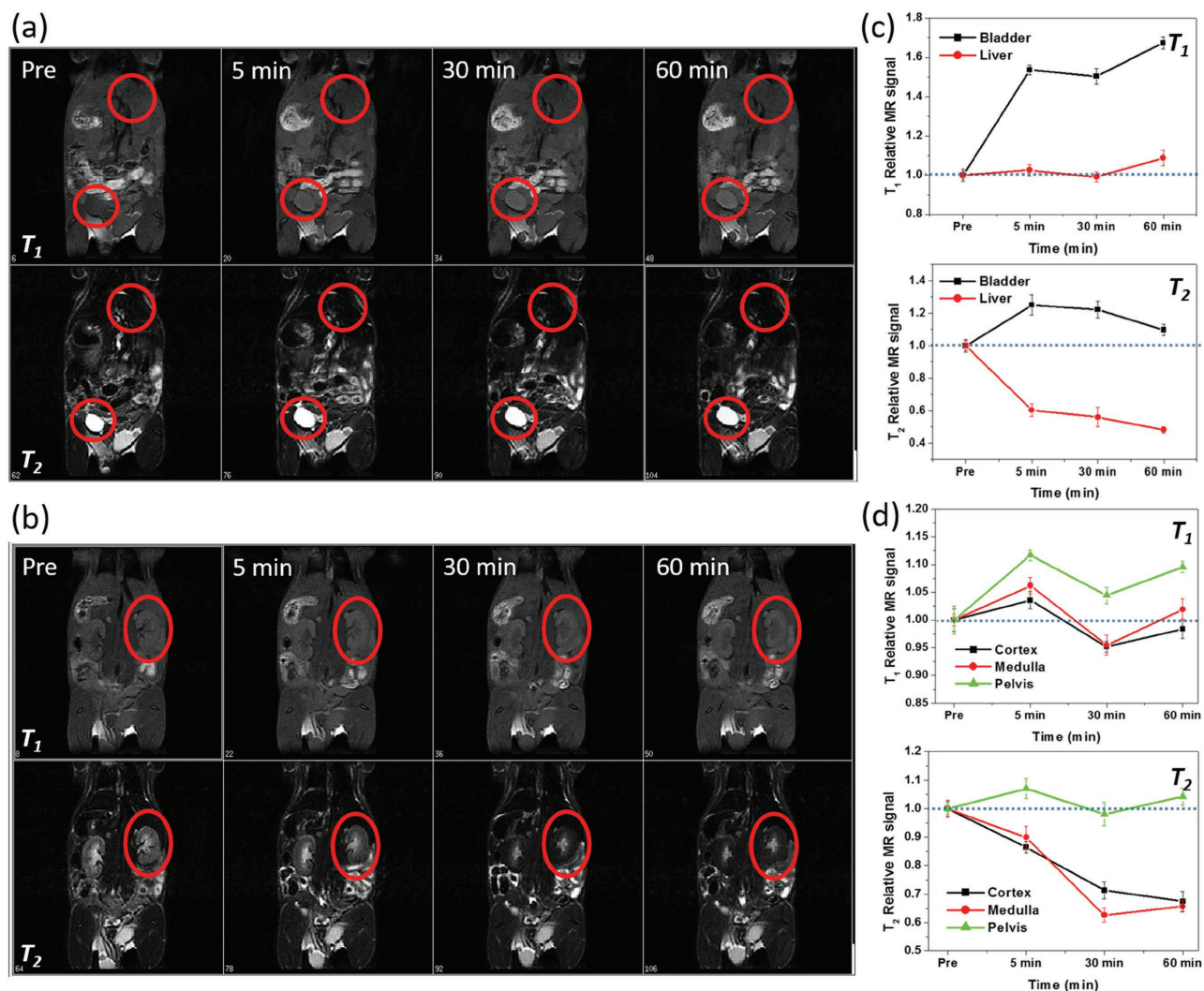


Figure 7. The T₁ and T₂ MR images of a) bladder and liver, b) kidney of mice administrated with FePt@mSiO₂@PDA-PEG at different time points. The signal to noise ratio of T₁ and T₂ MR imaging measurements in c) bladder and liver, and d) kidney.

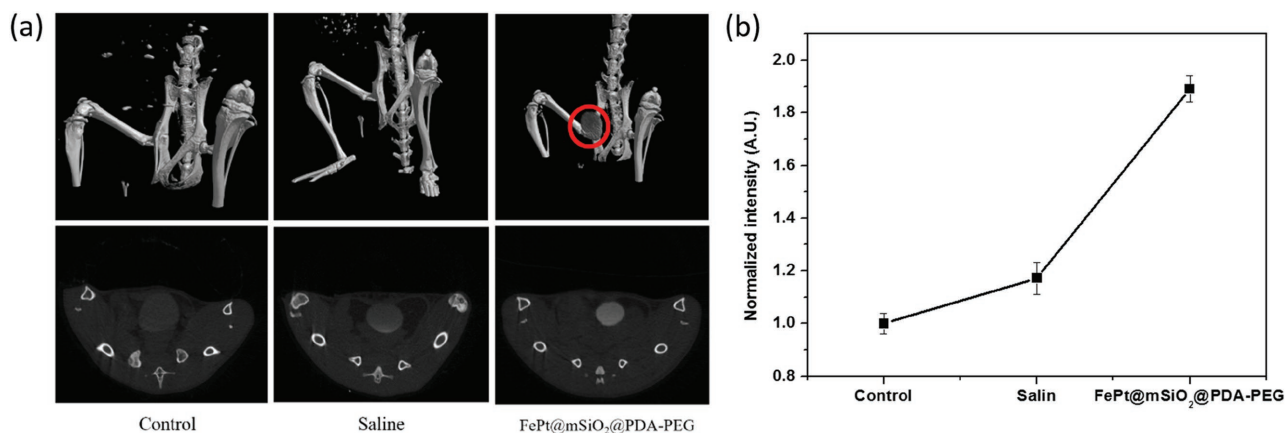


Figure 8. a) The in vivo 3D (upper) and 2D (lower) CT images of mice before injection (left), intravenously injected with saline solution (middle) and intravenously injected with FePt@mSiO₂@PDA-PEG. All the images were captured at 40 min. b) The signal intensity evaluation of bladder in the acquired CT image after tail-vein injection of FePt@mSiO₂@PDA-PEG NPs.

MR T_1 observation but also conquers the difficulty in bladder evaluation under MR T_2 mode (due to the bright background). The potential of this dual(T_1, T_2)-MRI/CT contrast agent in synergistic diagnosis is thus demonstrated.

Multiphoton irradiation offers several advantages over single photon luminescence, such as its deep tissue penetration, suppressed background noise and low photodamage.^[23] It also renders subcellular resolution and molecular sensitivity that compensate for MRI and CT. To further evaluate in vivo multiphoton imaging, FePt@mSiO₂@PDA-PEG was subcutaneously administrated in mouse back and observed with 850 nm femtosecond Ti:sapphire laser equipped on the Leica TCS SP5 MP. Before particle injection, the collagen (green) and sebaceous glands (yellow) network can be seen through second-harmonic generation contrast (Figure 9a,c). After particle injection, we clearly observed the distribution of FePt@mSiO₂@PDA-PEG both in the collagen network and near the sebaceous glands by two-photon microscopy (Figure 9b,d).

As polydopamine has been found to bind anticancer drugs easily through the π - π stacking interaction, providing a "molecular glue" environment for aromatic-ring-rich drugs.^[24] The potential of our FePt@mSiO₂@PDA-PEG in drug delivery was tested and shown in Figures S12 and S13 (Supporting Information). According to the calibration curve and the absorption spectrum of FePt@mSiO₂@PDA-PEG-DOX (Figure S12, Supporting Information), we calculated the DOX loaded on FePt@mSiO₂@PDA-PEG to be 103.86 $\mu\text{g mg}^{-1}$. Also, the corresponding cell viability was evaluated by MTT assay after treating FePt@mSiO₂@PDA-PEG-DOX for 15 h (Figure S13b, Supporting Information). Accordingly, cell viability was greatly reduced to 39.4% when 200 $\mu\text{g mL}^{-1}$ particle concentration

was introduced, suggesting the high drug loading capacity of FePt@mSiO₂@PDA-PEG-DOX.

On the other hand, as individual FePt^[15] or PDA^[25] has been reported to be a promising photothermal therapy agent for its relatively high efficient near-infrared (NIR) radiation absorption, we also evaluated the combination of these two materials in view of a photothermal therapeutic agent (Figure S14, Supporting Information). As shown in Figure S14 (Supporting Information), both final temperature of solution (Figure S14a, Supporting Information) and temperature elevation (Figure S14b, Supporting Information) are concentration dependent, which can achieve as high as 51.1 °C after irradiated for 13 min at 200 $\mu\text{g mL}^{-1}$. Although detailed in vivo experiments regarding to drug delivery and photothermal therapy are necessary to show its clinic usefulness, it is out of scope of this study.

3. Conclusion

In summary, mesoporous silica with high density of surface -OH concentration is found to facilitate heterogeneous nucleation of dopamine and therefore suppress dopamine random self-polymerization in water. Accordingly, a four-in-one (T_1 , T_2 , CT, MPL) imaging nanocomposite FePt@mSiO₂@PDA-PEG was strategically designed and synthesized, which, to the best of our knowledge, is the first paradigm to integrate CT and MPL component into MR dual-modes contrast agents. This nanoplat-form offers the advantages of (1) enhanced polydopamine-Fe³⁺ loading amount to improve the T_1 contrast (2) improved heterogeneous nucleation that prevent serious self-polymerization in water (3) delayed-biodegradation that renders the particle

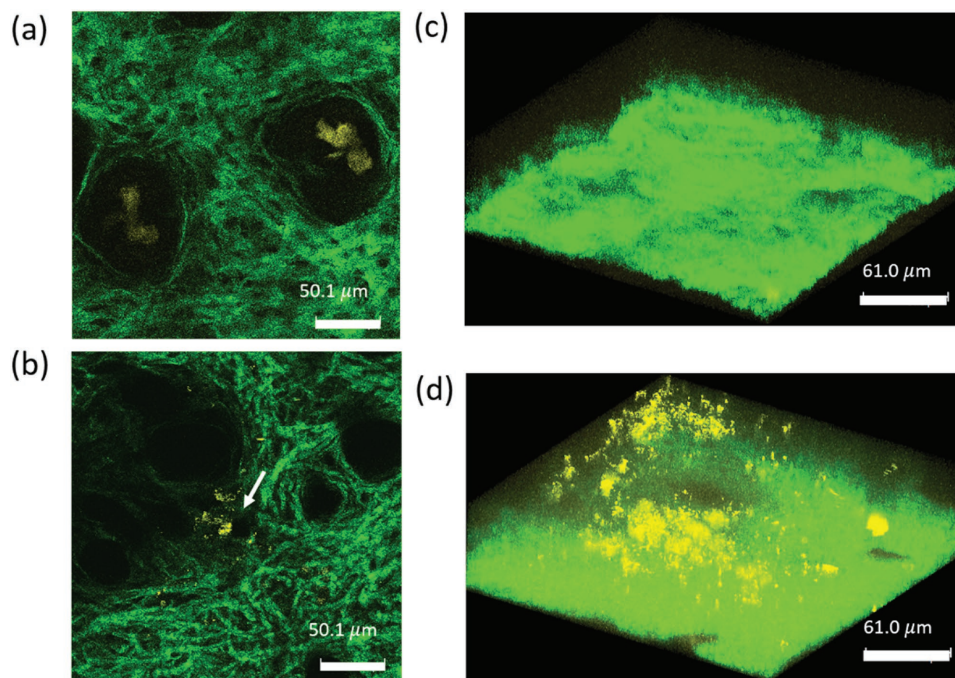


Figure 9. a) The in vivo multiphoton images of mice before injection and b) mice subcutaneously administrated with FePt@mSiO₂@PDA-PEG. c,d) Z-stacking images of (a) and (b), respectively.

integrity and avoids generation of silica fragments before excretion. It is for the first time that the biodegradation performance of polydopamine-Fe³⁺ in FBS is investigated. More importantly, assisted by the MR dual mode, we discovered a water-content-dependent manner in *in vivo* MR imaging, in which the bladder and pelvis in kidney showed enhancement in T₁-weighting MR imaging while T₂-weighted MR imaging is manifested in liver, medulla, and cortex, suggesting the importance of having T₁ and T₂ contrast in a single nanopatform for precise diagnosis. Also, the preliminary tests demonstrated the potentials of FePt@mSiO₂@PDA-PEG for drug delivery and photothermal therapy. Most importantly, according to our *in vivo* results, this dual(T₁,T₂)-MRI/CT contrast agent is demonstrated complementary to each other. These merits make mesoporous silica assisted deposition of bioinspired polydopamine onto FePt@mSiO₂ promising as a universal strategy to integrate multimodality for bioimaging.

4. Experimental Section

Chemicals: Absolute ethanol, hexane, ethyl acetate, and chloroform were used without further purification. Platinum acetylacetonate (Pt(acac)₂, ACROS, 97%), iron pentacarbonyl (Fe(CO)₅, Aldrich, 99%), hexadecane-1,2-diol (Aldrich, 90%), oleylamine (ACROS, C18 content 80%–90%), oleic acid (Aldrich, 70%), dioctyl ether (Aldrich, 90%), 1-octadecene (ACROS, 90%), CTAB, (ACROS, 99+%), tetraethyl orthosilicate (ACROS, 98%), dopamine hydrochloride (Aldrich), iron(III) chloride (FeCl₃, ACROS, 98%), mPEG-SH (Sigma, M_n = 6000), DOX HCl (DOX, AKSci, 98%).

Synthesis of FePt and Fe₃O₄ Nanoparticles: The FePt nanoparticles (≈11 nm) were synthesized according to previous report.^[15]

Synthesis of FePt@mSiO₂ Nanoparticles: To coat mesoporous silica shell onto the as-prepared FePt nanoparticle, a modified method reported previously was adopted.^[26] Briefly, 500 μL of the FePt nanoparticles in chloroform (6 mg mL⁻¹) was first added to 10 mL 0.1 M CTAB solution followed by sonication of the mixture to evaporate the chloroform. After the FePt nanoparticles were fully transferred into the CTAB solution, the mixture was then added into a solution containing 0.5 mL of 0.4 M NaOH, 29.5 mL water, 0.5 mL TEOS, and 3 mL ethyl acetate under vigorously stirred at 60 °C for 6 h. The as-synthesized materials were washed twice with ethanol and collected by centrifugation. To remove surfactant (CTAB) in the pores of mSiO₂, FePt@mSiO₂ NPs were transferred to 50 mL of ethanol solution containing NH₄NO₃ (300 mg) and vigorously stirred at 60 °C for 2 h.

Synthesis of FePt@SiO₂ and Fe₃O₄@SiO₂ Nanoparticles: The FePt@SiO₂ and Fe₃O₄@SiO₂ NPs were prepared by using a modified procedure reported previously.^[26] Briefly, cyclohexane (6 mL), Triton X-100 (1.5 mL), hexanol (1.2 mL), and water (250 μL) were added in sequence. FePt/Fe₃O₄ core nanoparticles dispersed in cyclohexane (2 mg mL⁻¹) were then added to the as-prepared mixture and vigorously stirred for 30 min. TEOS (25 μL) was added and kept stirring for another 1 h, followed by the addition of NH₄OH (50 μL) to initiate the hydrolysis–condensation reaction. The reaction was performed under room temperature and stopped by adding ethanol after stirring for 24 h. The core/shell nanoparticles were then collected by centrifugation (13 500 rpm) and redispersed in water for further use.

Surface Modification of PDA-PEG Layer: To incorporate T₁ imaging ability, dopamine hydrochloride (40 mg mL⁻¹) was added into FePt@mSiO₂ dispersed solution (1 mg mL⁻¹), followed by the addition of 50 μL 1 N NaOH(aq) under vigorous stirring. After 10 min of reacting, the products were collected by centrifugation (13 500 rpm) and washed twice with deionized (DI) water. The as-prepared FePt@mSiO₂@PDA NPs were then incubated with Fe³⁺ solution (1 mg mL⁻¹) and stirred for 3 h. The product was washed twice and purified by centrifugation.

To increase biocompatibility, the FePt@mSiO₂@PDA NPs were further modified with mPEG-SH (100 mg/1 mL) in Tris Buffer (pH = 8.5) and stirred for 12 h. The PEGylated nanoparticles were then retrieved by centrifugation (13 500 rpm) and washed three times with PBS buffer. The final product was stored in PBS buffer for further use.

DOX Loading for Drug Delivery: 1 mg of DOX was dispersed in 1 mL PBS buffer, and then mixed with FePt@mSiO₂@PDA-PEG solution (1 mg mL⁻¹) and stirred at 4 °C for 48 h, followed by centrifugation (13 500 rpm) and washed several times until no obvious color could be seen in the supernatant. The final product is denoted as FePt@mSiO₂@PDA-PEG-DOX in the following content.

Characterization: A JEOL 1230 transmission electron microscope (100 kV) was used to obtain TEM images. A 0.47 T Minispec spectrometer (Bruker Minispec mq series relaxometer) was used to measure the relaxivity; FTIR spectrum was collected with a Varian 640-IR spectrometer to determine the modification of ligands. Experiments of X-ray energy dispersive spectroscopy (EDS) were performed by using a GENESIS 2000 EDS detector connected to the high-resolution TEM instrument in order to confirm the chemical composition. Powder X-ray diffraction data were accessed on a Bruker AXS D2 PHASER diffractometer. The absorption spectrum of FePt@mSiO₂@PDA-PEG-DOX was measured using UV–vis spectrometry (HITACHI U-3310), and the absorption spectrum of FePt@mSiO₂@PDA-PEG was performed on UV–vis–NIR spectrometer V-570 (Jasco Inc.). XPS analyses were carried out in a XPS spectrometer (ULVAC-PHI 5000 VersaProbe) with a monochromatic Al Kα X-ray source (1486.6 eV) and its pass energy is 23.5 eV. SIMS measurements were conducted with a PHI TRIFT V nanoToF spectrometer. The selected primary ion is Bi₃²⁺, with its beam energy being 30 keV.

Relaxivity Measurement: The particles were dispersed in water with certain concentration (determined by ICP-MS) and the temperature was balanced to 40 °C before measurements of r₁ and r₂ relaxation times. Using a 0.47 T Minispec spectrometer (Bruker Minispec mq series relaxometer), r₂ relaxation times were determined through Carr–Purcell–Meiboom–Gill sequence, with recycle time 10 s, eight averages with phase cycling, and 180° pulse separation of 1 ms. To even echoes over 250 ms acquisition window, monoexponential fitting was applied and the r₁ relaxation was estimated using inversion recovery techniques with recycle time 10 s, four averages with phase cycling, and eight inversion times logarithmically spaced over the interval 0–2000 ms.

Multiphoton Measurement: Two-photon luminescence images of FePt@mSiO₂@PDA NPs were obtained using a Leica TCS SP5 MP equipped with a femtosecond Ti:sapphire laser and an optical parametric oscillator (OPO) that enables extension of excitation wavelength to 1–1.3 μm. The objective used in imaging was a 20×, 0.75 NA water-immersion objective (Leica). The corresponding fields of view were 255 μm × 255 μm with 512 × 512 pixels. Then, the luminescence intensity changes were monitored at different excitation powers. Through statistical analysis of the fluorescence images, an average intensity for each picture is obtained that can be used as a measure of the luminescence intensity. Three excitation wavelengths (850, 920, and 1250 nm) all resulted in luminescence signals of the nanoparticles.

In Vitro MR Imaging and CT Imaging: HeLa cells were treated with particles for 3 h, and were then washed and collected by centrifugation in test tubes. Tubes were then placed in a homemade water rack and tested under an 8 channel head coil. MRI was performed using a clinical 3 T MR system (Signal Excite, GE Healthcare). 2D T₁-weighted fast spin echo pulse sequences (repetition time (TR)/echo time (TE) = 550/13 ms) were used and the slice thickness was 1.0 mm with a 0.5 mm gap. The field of view (FOV) was 14 × 10 cm², and the matrix size was 288 × 192. Total scan time was 4 min and 5 s at the NEX (number of excitations) of 2. Analysis of images was performed at a workstation provided by GE Healthcare (Advantage workstation 4.2). To evaluate the imaging capability of FePt@mSiO₂@PDA-PEG in computed tomography, it was placed in Eppendorf tubes with serial dilution. The tubes were placed in a homemade rack and immersed in water. The rack was then transferred to a Sixty-four Multislice CT (Lightspeed VCT, GE Healthcare) and scanned under 80 keV, 100 mA, four times at the FOV of 32 cm. The

resolution was 512×512 and the slice thickness was 0.625 mm, under such a voxel is $0.625 \times 0.625 \times 0.625 \text{ cm}^3$, which is isotropic.

Cell Viability: The in vitro cytotoxicity test was carried out by using MTT (Roche) as colorimetric assay agent. The HeLa cells were seeded in a 96-well plate with cell density of 5×10^3 cells per well. 20 μL of FePt@mSiO₂@PDA-PEG in five different concentrations (20, 50, 100, 150, 200 $\mu\text{g mL}^{-1}$) were fed to cells, each was done with three replicates. After treating for 12 h, each well was washed with PBS twice and incubated in 200 μL of the culture medium with 10% MTT agent and was allowed to react for 4 h. After reaction completed, the culture medium was then removed and redispersed in 200 μL of dimethyl sulfoxide (Sigma-Aldrich) per well to dissolve the purple MTT formazan crystal. The absorbance was measured at 595 nm using an enzyme-linked immunosorbent assay (ELISA) reader (VersaMax Microplate Spectrophotometers, Molecular-Devices). Therapeutic efficiency of FePt@mSiO₂@PDA-PEG-DOX was also evaluated through MTT assay as described above.

Cell Labeling: 5×10^4 HeLa cells per well were cultivated in 6-well plate and treated with FePt@mSiO₂@PDA-PEG NPs (200 $\mu\text{g mL}^{-1}$) for 15 h. After removing the culture medium and washing twice with PBS, each well was incubated in 1% formaldehyde solution for 10 min, followed by addition of a mixed solution (equal amounts of 2 N hydrochloric acid and 2% potassium ferrocyanide solution) 200 μL per well and by 30 min of incubation. Each well was then washed with DI water and observed with an optical microscope (OLYMPUS IX81).

MRI In Vivo Experiment: All animals were anesthetized with 5% isoflurane at 1 L min^{-1} air flow. Upon fully anesthetized, the animal was placed in a prone position and fitted with a custom-designed head holder inside the magnet. Isoflurane was then maintained with 0.8%–1.2%, at 1 L min^{-1} air flow throughout the experiments. Mice body experiments were performed in a Biospec 4.7 T spectrometer before and at various time delay after the injection of FePt@mSiO₂@PDA-PEG with (T_1/T_2) TR = 500/5000 ms, (T_1/T_2) $T_{\text{eff}} = 10/70$ ms, FOV = 6 cm \times 6 cm, slice thickness = 1.0 mm, and matrix size = 256 \times 128 (zero-padded to 256 \times 256) with six replica. Typically, nanoparticles suspended in PBS buffer (0.1 mL) were administrated to BALB/c (LASCO, Taiwan) mice (7–9 weeks of age, body mass \approx 25 g) via tail vein injection at a dosage of 1 mg Fe kg^{-1} (body weight). The percentage of signal-to-noise (SNR) change for preinjection versus postinjection T_1 -weighted image and T_2 -weighted image was calculated according to the following formula: %SNR difference = $100 \times ((\text{SNR})_{\text{post}} - (\text{SNR})_{\text{pre}}) / (\text{SNR})_{\text{pre}}$.

CT In Vivo Experiment: The in vivo CT analysis was performed using Bruker Skyscan 1176. Imaging parameters were as follows: slice thickness, 35 mm; X-ray source voltage: 50.0 kV; X-ray source current: 500.0 μA ; field of view: 1000 \times 1000. Each image acquisition was performed when rotated one step (0.8°) through 360°. The images were processed for cross-sections by reconstruction using analysis software.

In Vivo Multiphoton Imaging: The BALB/c mouse was injected with 50 μL of FePt@mSiO₂@PDA-PEG NPs into the subcutaneous regions of the mouse back. The in vivo sectioning images of the nanoparticles were captured on a Leica TCS SP5 MP system equipped with a Ti:sapphire laser and an OPO. The multiphoton excitation wavelength was 850 nm. The objective used in imaging was a 20 \times , 0.75 NA water immersion objective (Leica).

Biodegradability Test: The as-prepared FePt@mSiO₂@PDA (2 mg) were incubated in PBS and FBS (1 mL) at 37 °C and images of samples were taken with TEM at series of time points to monitor the degradation. The mSiO₂, PDA, and PDA-Fe³⁺ were also mentioned to test their biodegradability as well.

Confocal Fluorescence Imaging: The HeLa cell were cultivated in a 6-well plate 5×10^4 cell per well in 2 mL of culture medium (without FBS) to promote the uptake of nanoparticles. After incubated for 2, 6, 15 h with 200 $\mu\text{g mL}^{-1}$ FePt@mSiO₂@PDA-DOX-PEG NPs, cells were then washed twice with PBS and fixed with 1% paraformaldehyde in PBS. To stain the nucleus, the cells were washed twice with PBS followed by addition of 10 $\mu\text{g mL}^{-1}$ 4',6-diamidino-2-phenylindole (Molecular Probes) for 5 min. The stained cells were then observed by a Zeiss LSM710 NLO confocal spectral microscope equipped with 63 \times (P-APO,1.40 oil

immersion) objective using 405 nm diode laser, 543 nm He-Ne laser as excitation source.

Photothermal Therapy Efficiency Evaluation: To evaluate the photothermal therapy efficiency of FePt@mSiO₂@PDA-PEG, different concentrations of FePt@mSiO₂@PDA-PEG were dispersed in DI water and transferred to a quartz cuvette, followed by irradiation of 808 nm laser (1 W cm^{-2}) for 800 s. A thermocouple probe was inserted into the solution and measured the temperature every 10 s.

Supporting Information

Supporting Information is available from the Wiley Online Library or from the author.

Acknowledgements

Y.-W.C. and Y.-K.P. contributed equally to this work. This work was supported by the Ministry of Science and Technology, Taiwan (MOST-104-2628-M-002013) and by grants from the AM2 Pharmacological Studies of Drugs in Animal Models for Human Diseases, Disease Animal Research Center, College of Medicine, National Taiwan University, the National Research Program for Biopharmaceuticals, National Science Council, Taiwan (Grant No. NSC-100-2325-B-002-060). The authors also thank the Taiwan Mouse Clinic (MOST 105-2325-B-001-010) which is funded by the National Research Program for Biopharmaceuticals (NRPB) at the Ministry of Science and Technology (MOST) of Taiwan for technical support in MRI in vivo experiment.

Received: December 21, 2016

Revised: February 7, 2017

Published online:

- [1] a) R. Weissleder, M. J. Pittet, *Nature* **2008**, *452*, 580; b) A. Louie, *Chem. Rev.* **2010**, *110*, 3146.
- [2] a) D. Kim, M. K. Yu, T. S. Lee, J. J. Park, Y. Y. Jeong, S. Jon, *Nanotechnology* **2011**, *22*, 155101; b) S.-W. Chou, Y.-H. Shau, P.-C. Wu, Y.-S. Yang, D.-B. Shieh, C.-C. Chen, *J. Am. Chem. Soc.* **2010**, *132*, 13270; c) W. Dong, Y. Li, D. Niu, Z. Ma, X. Liu, J. Gu, W. Zhao, Y. Zheng, J. Shi, *Small* **2013**, *9*, 2500.
- [3] a) S. Wen, K. Li, H. Cai, Q. Chen, M. Shen, Y. Huang, C. Peng, W. Hou, M. Zhu, G. Zhang, X. Shi, *Biomaterials* **2013**, *34*, 1570; b) H.-K. Kim, H.-Y. Jung, J.-A. Park, M.-I. Huh, J.-C. Jung, Y. Chang, T.-J. Kim, *J. Mater. Chem.* **2010**, *20*, 5411; c) C. Alric, J. Taleb, G. L. Duc, C. Mandon, C. Billotey, A. L. Meur-Herland, T. Brochard, F. Vocanson, M. Janier, P. Perriat, S. Roux, O. Tillement, *J. Am. Chem. Soc.* **2008**, *130*, 5908; d) Y.-J. Tseng, S.-W. Chou, J.-J. Shyue, S.-Y. Lin, J.-K. Hsiao, P.-T. Chou, *ACS Nano* **2016**, *10*, 5809; e) M. W. Ahmad, W. Xu, S. J. Kim, J. S. Baeck, Y. Chang, J. E. Bae, K. S. Chae, J. A. Park, T. J. Kim, G. H. Lee, *Sci. Rep.* **2015**, *5*, 8549.
- [4] F. Hu, Y. S. Zhao, *Nanoscale* **2012**, *4*, 6235.
- [5] a) J. G. Penfield, R. F. Reilly, *Nat. Clin. Pract. Nephrol.* **2007**, *3*, 654; b) E. A. Sadowski, L. K. Bennett, M. R. Chan, A. L. Wentland, A. L. Garrett, R. W. Garrett, A. Djamali, *Radiology* **2007**, *243*, 148.
- [6] a) T.-H. Shin, Y. Choi, S. Kim, J. Cheon, *Chem. Soc. Rev.* **2015**, *44*, 4501; b) N. A. Keasberry, M. Banobre-Lopez, C. Wood, G. J. Stasiuk, J. Gallo, N. J. Long, *Nanoscale* **2015**, *7*, 16119; c) D. Niu, X. Luo, Y. Li, X. Liu, X. Wang, J. Shi, *ACS Appl. Mater. Interfaces* **2013**, *5*, 9942; d) J.-S. Choi, J.-H. Lee, T.-H. Shin, H.-T. Song, E. Y. Kim, J. Cheon, *J. Am. Chem. Soc.* **2010**, *132*, 11015; e) K. H. Bae, Y. B. Kim, Y. Lee, J. Hwang, H. Park, T. G. Park, *Bioconjugate Chem.* **2010**, *21*, 505; f) Z. Zhou, D. Huang, J. Bao, Q. Chen, G. Liu,

- Z. Chen, X. Chen, J. Gao, *Adv. Mater.* **2012**, *24*, 6223; g) G. H. Im, S. M. Kim, D.-G. Lee, W. J. Lee, J. H. Lee, I. S. Lee, *Biomaterials* **2013**, *34*, 2069; h) T.-H. Shin, J.-S. Choi, S. Yun, I.-S. Kim, H.-T. Song, Y. Kim, K. I. Park, J. Cheon, *ACS Nano* **2014**, *8*, 3393; i) Y. Chen, K. Ai, J. Liu, X. Ren, C. Jiang, L. Lu, *Biomaterials* **2016**, *77*, 198.
- [7] D. Pan, S. D. Caruthers, A. Senpan, A. H. Schmieder, S. A. Wickline, G. M. Lanza, *Wiley Interdiscip. Rev.: Nanomed. Nanobiotechnol.* **2011**, *3*, 162.
- [8] Y.-K. Peng, C.-L. Liu, H.-C. Chen, S.-W. Chou, W.-H. Tseng, Y.-J. Tseng, C.-C. Kang, J.-K. Hsiao, P.-T. Chou, *J. Am. Chem. Soc.* **2013**, *135*, 18621.
- [9] Y.-K. Peng, S. C. E. Tsang, P.-T. Chou, *Mater. Today* **2016**, *19*, 336.
- [10] a) K. Y. Ju, J. W. Lee, G. H. Im, S. Lee, J. Pyo, S. B. Park, J. H. Lee, J. K. Lee, *Biomacromolecules* **2013**, *14*, 3491; b) Q. Fan, K. Cheng, X. Hu, X. Ma, R. Zhang, M. Yang, X. Lu, L. Xing, W. Huang, S. S. Gambhir, Z. Cheng, *J. Am. Chem. Soc.* **2014**, *136*, 15185; c) X. Wang, J. Zhang, Y. Wang, C. Wang, J. Xiao, Q. Zhang, Y. Cheng, *Biomaterials* **2016**, *81*, 114.
- [11] P. Caravan, J. J. Ellison, T. J. McMurry, R. B. Lauffer, *Chem. Rev.* **1999**, *99*, 2293.
- [12] a) F. Liu, X. He, Z. Lei, L. Liu, J. Zhang, H. You, H. Zhang, Z. Wang, *Adv. Healthcare Mater.* **2015**, *4*, 559; b) X. Ding, J. Liu, J. Li, F. Wang, Y. Wang, S. Song, H. Zhang, *Chem. Sci.* **2016**, *7*, 6695.
- [13] H. L. Ding, Y. X. Zhang, S. Wang, J. M. Xu, S. C. Xu, G. H. Li, *Chem. Mater.* **2012**, *24*, 4572.
- [14] a) X. Liu, J. Cao, H. Li, J. Li, Q. Jin, K. Ren, J. Ji, *ACS Nano* **2013**, *7*, 9384; b) L.-S. Lin, Z.-X. Cong, J.-B. Cao, K.-M. Ke, Q.-L. Peng, J. Gao, H.-H. Yang, G. Liu, X. Chen, *ACS Nano* **2014**, *8*, 3876; c) J. Park, T. F. Brust, H. J. Lee, S. C. Lee, V. J. Watts, Y. Yeo, *ACS Nano* **2014**, *8*, 3347; d) J. Zhou, B. Duan, Z. Fang, J. Song, C. Wang, P. B. Messersmith, H. Duan, *Adv. Mater.* **2014**, *26*, 701; e) J. Zhou, P. Wang, C. Wang, Y. T. Goh, Z. Fang, P. B. Messersmith, H. Duan, *ACS Nano* **2015**, *9*, 6951.
- [15] S.-W. Chou, C.-L. Liu, T.-M. Liu, Y.-F. Shen, L.-C. Kuo, C.-H. Wu, T.-Y. Hsieh, P.-C. Wu, M.-R. Tsai, C.-C. Yang, K.-Y. Chang, M.-H. Lu, P.-C. Li, S.-P. Chen, Y.-H. Wang, C.-W. Lu, Y.-A. Chen, C.-C. Huang, C.-R. C. Wang, J.-K. Hsiao, M.-L. Li, P.-T. Chou, *Biomaterials* **2016**, *85*, 54.
- [16] H. Lee, S. M. Dellatore, W. M. Miller, P. B. Messersmith, *Science* **2007**, *318*, 426.
- [17] a) T. López, P. Quintana, J. M. Martínez, D. Esquivel, *J. Non-Cryst. Solids* **2007**, *353*, 987; b) C.-C. Ho, S.-J. Ding, *Chem. Commun.* **2014**, *50*, 3602.
- [18] J. N. Masi, D. Newitt, C. A. Sell, H. Daldrup-Link, L. Steinbach, S. Majumdar, T. M. Link, *Am. J. Roentgenol.* **2005**, *184*, 1754.
- [19] K. K. Pohaku Mitchell, A. Liberman, A. C. Kummel, W. C. Trogler, *J. Am. Chem. Soc.* **2012**, *134*, 13997.
- [20] Y.-K. Peng, Y.-J. Tseng, C.-L. Liu, S.-W. Chou, Y.-W. Chen, S. C. E. Tsang, P.-T. Chou, *Nanoscale* **2015**, *7*, 2676.
- [21] L. Hong, J. D. Simon, *J. Phys. Chem. B* **2007**, *111*, 7938.
- [22] J. V. Jokerst, T. Lobovkina, R. N. Zare, S. S. Gambhir, *Nanomedicine* **2011**, *6*, 715.
- [23] W. Denk, K. Svoboda, *Neuron* **1997**, *18*, 351.
- [24] R. Zhang, Q. Fan, M. Yang, K. Cheng, X. Lu, L. Zhang, W. Huang, Z. Cheng, *Adv. Mater.* **2015**, *27*, 5063.
- [25] Y. Liu, K. Ai, J. Liu, M. Deng, Y. He, L. Lu, *Adv. Mater.* **2013**, *25*, 1353.
- [26] Y.-K. Peng, C.-W. Lai, C.-L. Liu, H.-C. Chen, Y.-H. Hsiao, W.-L. Liu, K.-C. Tang, Y. Chi, J.-K. Hsiao, K.-E. Lim, H.-E. Liao, J.-J. Shyue, P.-T. Chou, *ACS Nano* **2011**, *5*, 4177.